Journal of Advanced Ceramics
先进陶瓷
ISSN 2226-4108
CN 10-1154/TQ
清華大學出版社 Tsinghua University Press
SciOpen

J Adv Ceram 2026, **15**: 9221375

https://doi.org/10.26599/JAC.2026.9221375

Research Article

Regulating d-band center and d-p orbital alignment to enhance K_2NiF_4-type cathode performance for protonic ceramic fuel cells

Zhe Song[#], Shaozhi Wang[#], Dezhi Geng, Zhangjin Xie, Shenchi Qu, Jie Hou[*]

School of Resource Environment and Safety Engineering, University of South China, Hengyang 421001, China

[#]Zhe Song and Shaozhi Wang contributed equally to this work.

* Corresponding author.

E-mail: jiehou@usc.edu.cn

Received: June 16, 2026; Revised: August 7, 2026; Accepted: September 9, 2026

Abstract: Regulating the transition-metal d-band center and metal-oxygen orbital alignment represents a potentially useful approach to improve cathodic oxygen reduction reaction (ORR) kinetics in

protonic ceramic fuel cells (PCFCs). Herein, K_2NiF_4-type $La_{0.5}Sr_{1.5}MnO_{4+\delta}$ (LSMO) and Fe-based $La_{0.5}Sr_{1.5}FeO_{4+\delta}$ (LSFO) cathodes were investigated to clarify how electronic-structure regulation affects oxygen-defect chemistry, oxygen/proton transport, and proton-involved ORR activity. Density functional theory (DFT) calculations reveal that the work-function difference between LSFO and LSMO is negligible, whereas LSFO possesses a more favorable Fe 3d-O 2p energy alignment. This electronic configuration lowers the energetic cost of oxygen-vacancy formation, improves hydration-related proton incorporation, reduces the proton-hopping barrier, and decreases the free-energy barrier for key ORR intermediates. Experimentally, LSFO exhibits enriched oxygen-vacancy-related surface oxygen species, much higher electronic conductivity, and accelerated oxygen/proton surface exchange and diffusion. P_{O2}/P_{H2O}-dependent electrochemical impedance spectra further confirm that LSFO promotes multiple p-ORR sub-processes, including interfacial charge/proton transfer, oxygen reduction, and surface oxygen transport. Consequently, the optimized LSFO cathode achieves a peak power density of 2.2 W cm^{-2} and a polarization resistance of 0.04 Ω cm^2 at 700 °C, outperforming LSMO and many reported R-P cathodes. Moreover, the LSFO cell exhibits stable operation over 400 h. These results demonstrate that coordinated regulation of the d-band center and d-p orbital alignment is a viable way to design high-performance K_2NiF_4-type PCFC cathodes.

Keywords: Protonic ceramic fuel cells: d-band center: Oxygen reduction reaction; Electrocatalysis; K_2NiF_4-type

1 Introduction

Rising global energy demands and environmental imperatives are driving the development of sustainable electrochemical conversion technologies. Solid oxide fuel cells (SOFCs), characterized by high efficiency, fuel flexibility (H_2, CH_4, CO, NH_3, etc.), near-zero emissions, and an all-solid, noble-metal-free architecture, represent a leading solution for decarbonized power generation [1-6]. As an evolution of SOFC technology, protonic ceramic fuel cells (PCFCs) are emerging as highly efficient

energy-conversion devices operating at intermediate temperatures (typically 300-700 °C), mitigating material degradation and enabling the use of cost-effective metallic interconnects [7, 8]. In a PCFC, protons conduct through a ceramic electrolyte and react with oxygen at the cathode to form water [8-10]. The performance of PCFCs is predominantly limited by the cathode, where the proton-involved oxygen reduction reaction (p-ORR) must occur efficiently [9, 11, 12]. Unlike conventional oxygen-conducting SOFCs, PCFC cathodes must facilitate electron and oxide-ion transport while also incorporating protons, making them triple-conducting mixed ionic-electronic conductors (MIECs) [13]. In practice, low catalytic activity at reduced temperatures and the complexity of multi-ion transport lead to sluggish cathode kinetics [14, 15]. Consequently, high performance requires cathode materials that combine rapid ORR kinetics, high proton and oxide-ion conductivity, thermal and chemical compatibility with the electrolyte, and long-term stability. The challenge of meeting all these demands underscores the importance of advancing cathode materials in PCFC research.

Numerous cathode materials for PCFCs have been proposed, with perovskite oxides being the most widely investigated [8, 16]. These high-performance perovskite-based cathodes have significantly enhanced PCFC efficiency. However, challenges such as mismatched thermal expansion coefficients, chemical instability, and elemental segregation undermine their long-term stability and performance, thereby prompting the investigation of alternative cathode materials. K_2NiF_4-type Ruddlesden-Popper (R-P) phase materials (A_2BO_4) have emerged as promising candidates due to their superior oxygen diffusivity, fast surface exchange kinetics, and thermal expansion compatibility with common electrolytes [17-19]. Their layered structure, comprising of alternating perovskite and rock-salt layers, allows these materials to accommodate high oxygen non-stoichiometry and facilitate proton uptake, which is crucial for PCFC operation. Despite these advantages, their electrochemical performance still falls short of that observed in perovskite-based materials, highlighting the need for further optimization to enhance their practical performance.

Electronic-structure regulation, particularly the tuning of the transition-metal d-band center and metal-oxygen orbital alignment, has been widely used to optimize the adsorption and activation of oxygen-containing intermediates. In metal catalysts (e.g. Pt or Pd alloys), the d-band center is a well-established descriptor for the binding strength of oxygen species [20-22]. Similar concepts have also been extended to oxide electrodes, where the relative positions of transition-metal 3d and O 2p states influence metal-oxygen covalency, oxygen-redox activity, defect formation, and ORR/oxygen evolution reaction (OER) intermediate energetics [23, 24]. However, most previous studies on d-band regulation have focused on ORR/OER in liquid-electrolyte systems, zinc-air batteries, or catalytic oxidation of volatile organic compounds, where the reaction environments and rate-determining processes differ substantially from those in PCFC cathodes. In PCFCs, oxygen reduction occurs in humid oxygen and is coupled with proton incorporation, oxygen-defect formation, and water generation at the cathode surface. Even so, a simple upward or downward shift of the d-band center is insufficient to describe the activity trend. Instead, an optimized d-band center should be considered together with the transition-metal 3d-O 2p energy separation, oxygen-sublattice redox ability, and defect thermodynamics. Establishing this electronic-structure/defect-chemistry relationship is critical for rationally designing R-P cathodes with fast p-ORR kinetics.

In this context, we use a DFT-guided strategy to identify Fe-based K_2NiF_4-type $La_{0.5}Sr_{1.5}FeO_{4+\delta}$ (LSFO) as a promising cathode derived from the underexplored $La_{2-x}Sr_xBO_{4+\delta}$ family, with Mn-based $La_{0.5}Sr_{1.5}MnO_{4+\delta}$ (LSMO) selected as the reference composition for its structural robustness and moderate electrochemical activity. It extends the established d-band-center descriptor to p-ORR in layered K_2NiF_4-type PCFC cathodes by integrating it with d-p alignment, oxygen-redox behavior, and defect thermodynamics. By comparing LSMO and LSFO, we aim to clarify how B-site electronic-structure regulation affects oxygen-vacancy formation, interstitial-oxygen accommodation, hydration thermodynamics, proton migration, and surface ORR energetics under PCFC-relevant conditions. $La_{0.4}Sr_{1.6}FeO_{4+\delta}$ (LSFO-04) and $La_{0.6}Sr_{1.4}FeO_{4+\delta}$ (LSFO-06) were also synthesized as composition

controls bracketing LSFO to assess how La/Sr variations affect Fe valence, lattice/defect chemistry, and oxygen/proton transport, thereby identifying a balanced Fe-based composition. The study integrates DFT calculations, structural characterization, surface chemical analysis, oxygen/proton electrical conductivity relaxation (ECR), P_{O2}/P_{H2O}-dependent impedance analysis, and single-cell testing. Accordingly, it establishes and experimentally validates an electronic structure-defect-transport relationship governing p-ORR kinetics and PCFC performance in K_2NiF_4-type cathodes.

2 Experimental section

$BaZr_{0.1}Ce_{0.7}Y_{0.2}O_{3-\delta}$ (BZCY) and K_2NiF_4-structured oxides (LSMO, LSFO-04, LSFO, LSFO-06) were synthesized using the citric acid-nitrate gel combustion method [25]. The precursors were calcined at 1000 °C in air for 3 h to achieve phase purification and produce well-crystallized powders. Phase identification was conducted via X-ray diffraction (XRD, DX-2700BH), while morphology, crystallinity and surface chemical compositions were analyzed by transmission electron microscopy (TEM, Tecnai G2 F20, 200 kV) and X-ray photoelectron spectroscopy (XPS, Thermo Scientific K-Alpha), respectively. Dense bar-shaped LSMO, LSFO-04, LSFO and LSFO-06 samples with dimensions of approximately 40 mm × 5 mm × 2 mm were prepared by dry-pressing the powders in a stainless-steel mold and sintered at 1400 °C for 5 h. ECR measurements were subsequently performed using four-probe method [26] under controlled atmosphere transitions: air to oxygen (50% N_2 balance) or dry air to humidified air (3% H_2O). Conductivity transients were recorded until steady-state equilibrium was reached. The ECR data were analyzed using well-established diffusion models [27, 28] to extract oxygen/proton surface exchange coefficients (K) and bulk diffusion coefficients (D), enabling a systematic evaluation of ionic transport properties. K mainly describes the effective surface exchange and incorporation process, whereas D represents chemical transport. All samples had comparable geometries and were analyzed using the same fitting procedure, minimizing geometry-related differences among the compositions.

First-principles calculations were performed using density functional theory (DFT), as implemented

in the Vienna ab initio simulation package (VASP) [29]. The exchange-correlation potential was described by the Perdew-Burke-Ernzerhof (PBE) generalized gradient approach (GGA), and electron-ion interactions were modeled using the projector augmented wave (PAW) method. The following computational parameters were used: an energy convergence threshold of 10^{-4} eV, a force convergence criterion of 0.05 eV $Å^{-1}$, a plane-wave cutoff energy of 520 eV and a 3 × 3 × 1 k-point grid for the Brillouin zone. The oxygen vacancy formation energy (E_{V_O}) and the interstitial oxygen formation energy (E_{io}) were calculated according to the formulas $E_{Vo} = E_{defect} + \frac{1}{2}E_{O_2} - E_{perfect}$ and $E_{io} = E_{O,plus} - \frac{1}{2}E_{O_2} - E_{perfect}$ (E_{defect}: energy of a defective bulk, $E_{O,plus}$: energy of a bulk with one plus atom O, E_{O_2}: total energy of oxygen molecule, $E_{perfect}$: energy of perfect bulk). The hydration energy was computed based on the incorporation mechanism $H_2O + V_O^{\bullet\bullet} + O_O^{\times} \leftrightarrow 2OH^{\bullet}$, using the formula $E_{hydration} = E_{2OH} - E_{H_2O} - E_{defect}$ (E_{2OH}: energy of hydrated bulk, E_{H_2O}: energy of a water molecular, E_{defect}: energy of one oxygen atom removed bulk). To investigate the surface ORR energies, the (001) surface was cleaved with an added 15 Å vacuum layer. During the calculations, the top two layers were allowed to fully relax, while the bottom four layers were kept fixed. Gibbs free energies for ORR were calculated by determining the total energy of the system and incorporating entropy changes (TΔS).

ORR activities were assessed using symmetrical cell configurations with BZCY substrates, fabricated via die-pressing BZCY powders and sintering at 1500 °C for 6 h in air. Single cells were assembled with co-sintered (1350 °C, 6 h) bilayer of BZCY electrolyte and NiO-BZCY anode (65:35 wt% ratio), and screen-printed LSMO or LSFO cathode slurries (obtained by mixing with 10 wt% ethylcellulose-terpineol), which were sintered 1000 °C for 3 h to establish porosity. The cathode area is 0.196 cm^{-2}. Cathodes were applied to both sides of BZCY substrates and NiO-BZCY|BZCY half-cells using the same method. For optimized parameters, LSFO cathode were also assembled at 900 and 1100 °C for 3h, which were assessed comparably. Electrochemical impedance spectroscopy (EIS)

was conducted under various atmospheres to assess ORR kinetics in symmetrical cell configurations. For single-cell characterization, operando electrochemical testing was performed using a four-probe setup (Squidstat Plus, Admiral Instruments), with gas flow conditions of humidified H_2 (3% H_2O, 30 mL min^{-1}) as fuel and static air as oxidant. Performance evaluation was conducted using linear sweep voltammetry (LSV) mode (P-I/V-I curves) and EIS (0.1 Hz-1 MHz, 5 mV AC amplitude, open-circuit voltage) with silver paste and wires as current collection. Post-test cell microstructure analysis was examined using scanning electron microscopy (SEM, Phenom XL G2).

3 Results and discussion

3.1 DFT-guided identification of LSFO as a promising R-P cathode

The surface electronic structures of LSFO and LSMO were first analyzed to identify the intrinsic origin of their different cathodic activities. As shown in Fig. 1(a)-(b), LSFO exhibits a work function of 2.777 eV, which is only marginally higher than that of LSMO (2.768 eV). Given the very small difference, the two materials should be considered to possess essentially comparable surface electron-removal energetics. Therefore, work function is unlikely to be the dominant descriptor responsible for their markedly different cathodic activities, although its possible contribution to interfacial charge transfer and adsorption processes cannot be completely excluded. Instead, the enhanced ORR activity of LSFO is mainly associated with the distinct electronic configuration generated by Fe-based B-site chemistry. The lower Fermi level of LSFO reflects a reduced electronic chemical potential, but its catalytic implication should be interpreted together with the Fe 3d-O 2p interaction and defect thermodynamics rather than as an isolated descriptor. Compared with LSMO, LSFO provides an electronic environment more favorable for oxygen-sublattice participation and oxygen-defect stabilization, which is essential for vacancy-mediated oxygen exchange and p-ORR kinetics.

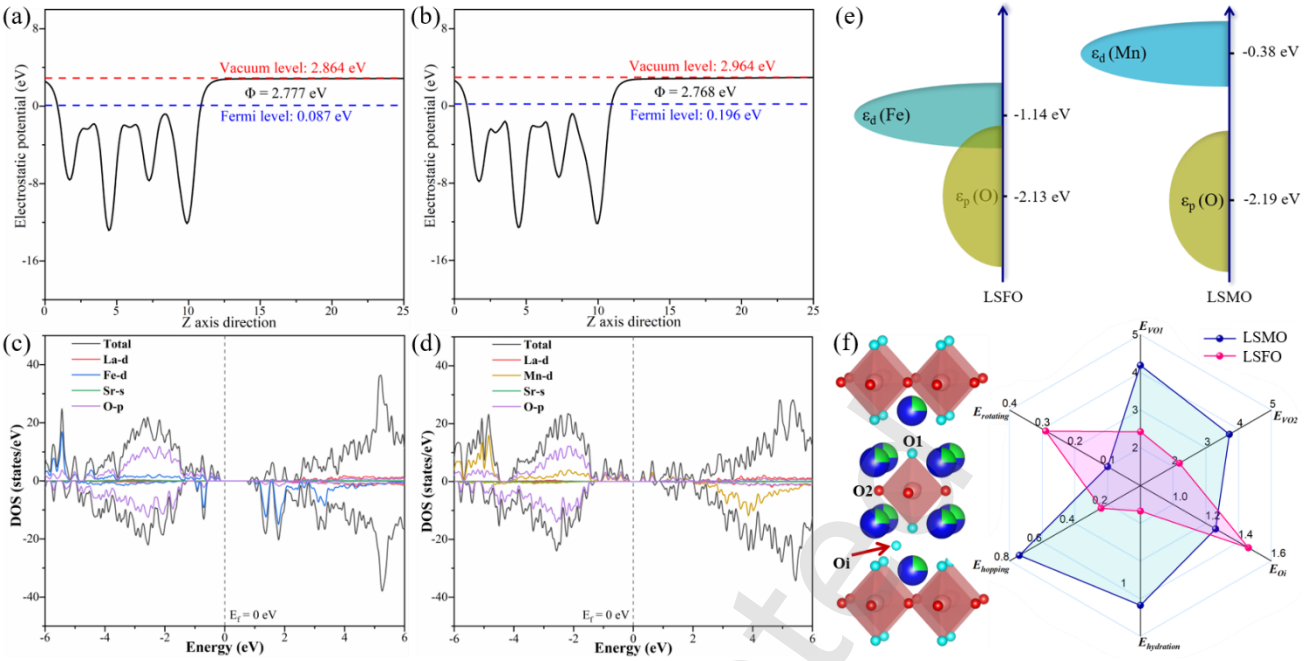

Fig. 1 Analysis by DFT calculations. Plane-averaged electrostatic potential profiles along the surface normal for (a) LSFO and (b) LSMO with the corresponding work function (Φ), based on the structure shown in Fig. S1; spin-polarized total and projected density of states (PDOS) of (c) LSFO and (d) LSMO (Fig. S2); (e) schematic band alignment illustrating the relative positions of the d-band centers (ε_d) for Fe and Mn, and O p-band center (ε_p) in LSFO and LSMO; (f) illustration of O1, O2 and Oi sites in the K_2NiF_4-type lattice, and comparison of key DFT-derived properties for LSFO and LSMO based on the optimized models (Fig. S3).

The d-band centers of LSFO and LSMO were determined by integrating Fe 3d and Mn 3d projected density of states (PDOS) within a fixed energy window around the Fermi level, which further reveal that the enhanced activity of LSFO is associated with its distinct Fe 3d-O 2p orbital alignment and the resulting differences in oxygen-defect and proton-transfer energetics. As shown in Fig. 1(c) and Table S1, in LSFO, the Fe 3d and O 2p states show substantial overlap below the Fermi level, indicating stronger Fe-O covalency interaction and efficient d-p hybridization [24, 30]. Such electronic coupling favors charge redistribution between Fe cations and the oxygen sublattice during ORR, thereby stabilizing oxygen-derived intermediates and facilitating lattice-oxygen participation. By contrast, although the Mn 3d states in LSMO are closer to the Fermi level, their overlap with O 2p states is weaker (Fig. 1(d) and Table S1), leading to more localized electronic states and less efficient stabilization of oxygen defects [24]. Additionally, the schematic band alignment in Fig. 1(e) shows

that, in LSFO, the Fe d-band center ($\varepsilon_d = -1.14$ eV) lies closer to the O 2p band center ($\varepsilon_p = -2.13$ eV), resulting in a smaller d-p energy separation. This favorable d-p alignment promotes oxygen-hole delocalization and oxygen-redox activity, whereas the larger d-p separation in LSMO (ε_d = -0.38 eV and $\varepsilon_p = -2.19$ eV) weakens Mn-O hybridization and limits oxygen-vacancy stabilization. Thus, the activity advantage of LSFO should be described as the consequence of coordinated d-band center regulation and Fe 3d-O 2p alignment, together with favorable oxygen-redox behavior and defect thermodynamics.

The DFT-derived defect and proton-transfer energetics provide a direct link between electronic-structure regulation and PCFC-relevant reaction kinetics. As summarized in Fig. 1(f) and Table S1, two crystallographically distinct oxygen sites, O1 and O2, were considered to account for their different local coordination environments around the BO_6 octahedra and oxygen-vacancy formation tendencies in the layered K_2NiF_4 lattice. This site-dependent analysis provides a more representative assessment of oxygen-defect formation and the local oxygen-sublattice activity. The E_{VO} for LSFO ($E_{VO1} = 2.43$ eV, $E_{VO2} = 2.19$ eV) are substantially lower than those of LSMO ($E_{VO1} = 4.19$ eV, $E_{VO2} = 3.72$ eV). These results directly indicates that oxygen vacancies can be generated and stabilized more readily in the Fe-based lattice. These vacancies serve as active sites for oxygen adsorption, dissociation, incorporation, and subsequent charge transfer. In comparison, the calculated interstitial oxygen formation energies (E_{Oi}) of LSFO and LSMO are relatively close (1.46 and 1.26 eV for LSFO and LSMO), indicating that the major improvement in LSFO arises mainly from vacancy-mediated oxygen exchange rather than from a dominant interstitial-oxygen pathway, which does not exclude possible interstitial-oxygen participation but identifies vacancy-related defect chemistry as the principal origin of the improvement of LSFO relative to LSMO. Hydration and proton migration are also critical for PCFC cathodes. The hydration energy ($E_{hydration}$) of LSFO is 0.27 eV, lower than that of LSMO (1.27 eV), indicating that proton incorporation through hydration is easier in LSFO under the adopted calculation scheme. Although both hydration energies are positive, the lower value of LSFO suggests a reduced energy penalty for water incorporation and hydroxyl-defect formation compared with LSMO. Therefore, LSFO possesses enhanced hydration capability on a comparative basis. Proton migration was further evaluated using the CI-NEB method by considering a hopping and rotating mechanism (Fig. S4). Protons incorporated as hydroxyl defects first rotate around the host

oxygen and then hop to a neighboring oxygen through a transient O-H···O configuration. Repeated rotation-hopping steps enable migration through the connected oxygen sublattice of the layered K_2NiF_4 structure. The migration barrier is affected by the local octahedral structure and oxygen-sublattice electronic structure. FeO_6 distortion may modify the O···O distance and orientation, while the smaller Fe 3d-O 2p energy separation and stronger Fe-O hybridization in LSFO may facilitate charge redistribution during proton transfer. Accordingly, although LSFO exhibits a slightly higher proton rotation barrier than LSMO (0.29 eV vs. 0.1 eV), its proton hopping barrier is dramatically reduced from 0.74 eV in LSMO to 0.24 eV in LSFO. For long-range proton diffusion is strongly governed by successive hopping events; therefore, the reduced hopping barrier is expected to accelerate proton transport in LSFO. Overall, LSFO is predicted to exhibit faster p-ORR kinetics because its Fe-based electronic structure simultaneously promotes oxygen-vacancy formation, hydration-related proton incorporation, proton migration, and lattice-oxygen-assisted ORR activity.

3.2 Structural confirmation and chemical compatibility of LSFO-based oxide

After the DFT-guided identification of LSFO, the phase structure and microstructure of the synthesized oxides were examined. As illustrated in Fig. 2(a), the XRD patterns for LSFO-04, LSFO, LSFO-06, and LSMO exhibit distinct peaks, which are characteristic of the tetragonal K_2NiF_4-type structure with the I4/mmm space group, confirming the successful synthesis of these oxides. Notably, the (004) diffraction peak shows a slight low-angle shift from LSFO-04 to LSFO-06, while the (110) diffraction peak remains virtually unchanged (Fig. S5), suggesting an elongation of the structure along the c-axis (Fig. S6). This structural evolution can be associated with the progressive increase in La^{3+} content and the accompanying change in the average Fe valence state, which affects FeO_6 octahedral size and the local layered framework. XRD Rietveld refinement (Fig. 2(b)) demonstrates an excellent match between the experimental and simulated patterns (blue tick marks and green residual curve), with low R_{wp} (weighted profile factor) and reduced chi-square values, further substantiating the phase purity of the materials. In contrast to LSMO, the XRD peaks of LSFO show both high- and low-angle shifts (Fig. 2(c) and Table S2), implying anisotropic lattice deformation induced by B-site replacement. Importantly, all synthesized materials exhibit excellent chemical compatibility with the BZCY electrolyte, retaining their phase purity after co-sintering at 1000 °C for 3 h (Fig. S7). Additionally, as

shown in Fig. 2(d), LSFO particles possess a submicron morphology with sizes ranging from 100 to 240 nm, which is advantageous for fabricating porous cathodes to facilitate gas transport and promote electrochemical reactions. Energy-dispersive X-ray spectroscopy (EDS) mapping indicates a uniform distribution of La, Sr, Fe, and O, confirming stoichiometric homogeneity at the microscale. SAED analysis (Fig. 2(e)) reveals high crystallinity, with lattice spacings of 2.72 Å (110), 1.92 Å (200), 1.34 Å (220), and 1.22 Å (310). HRTEM further corroborates these lattice spacing values, particularly 2.72 Å (110) and 1.92 Å (200) (Fig. 2(f)). Collectively, these results confirm the structural integrity and compositional homogeneity of LSFO, providing a reliable basis for evaluating the electronic and electrochemical effects.

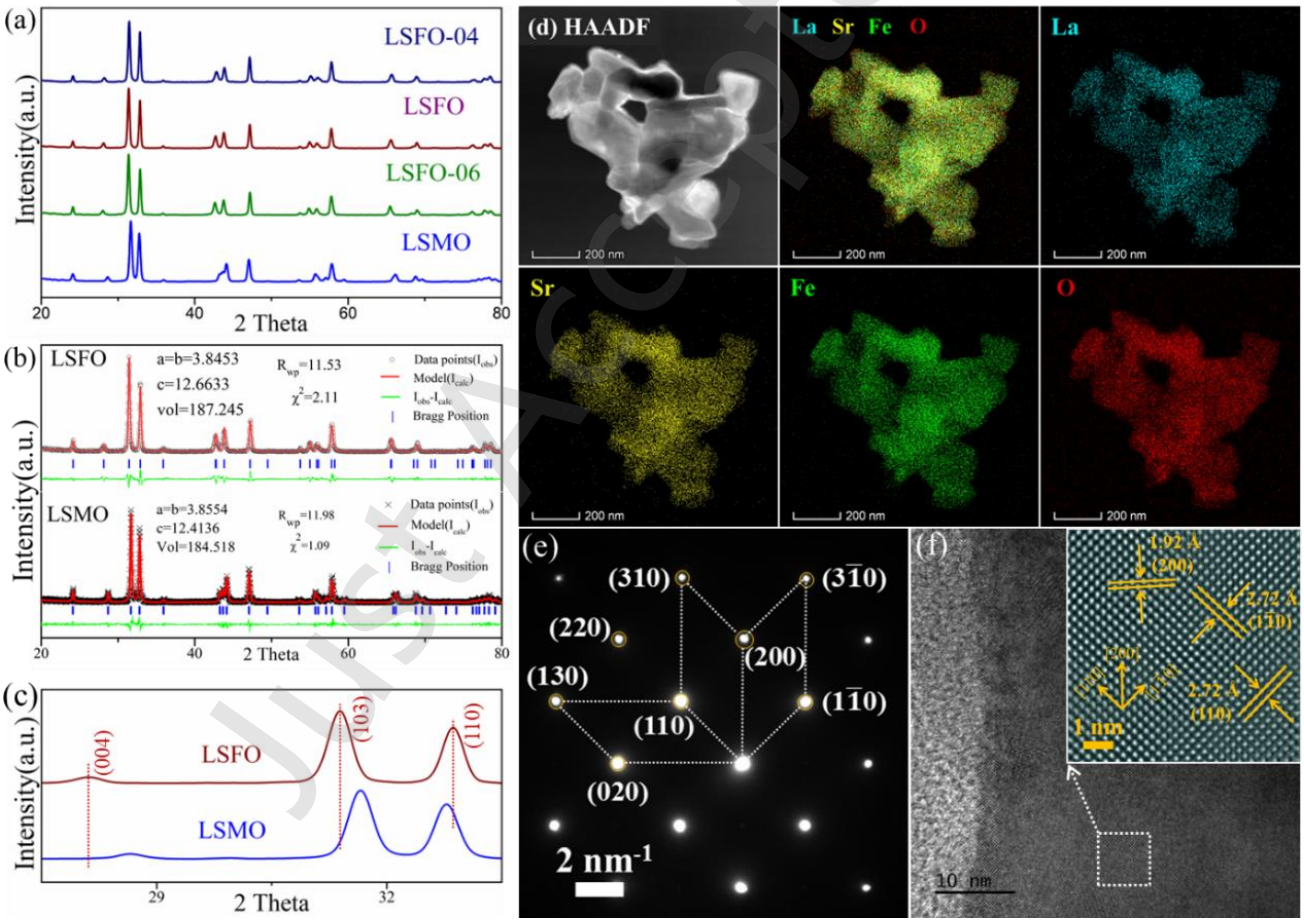

Fig. 2 Structural and microstructural characterization. (a) XRD patterns of LSFO-04, LSFO, LSFO-06, and LSMO fired at 1000 °C for 3h; (b) XRD Rietveld refinements of LSFO and LSMO, and (c) the comparison at 27.5-31.5°; (d) TEM HADDF images of LSFO with elemental mapping; (e) selected

area electron diffraction (SAED) patterns; (f) HRTEM image with the corresponding FFT iamge showing representative lattice planes.

3.3 Experimental validation of defect chemistry and oxygen/proton transport

XPS, EC, and ECR measurements were then used to experimentally verify the DFT-predicted differences in defect chemistry and ion-transport kinetics. The Fe *2p* XPS spectra of the LSFO series (Fig. 3(a)) can be deconvoluted into components assignable to mixed $Fe^{2+}/Fe^{3+}/Fe^{4+}$ surface species [31, 32] with varying proportions among the samples (Table S3), suggesting flexible redox compensation in the Fe-based lattice. The increase in Fe^{2+} contribution and decrease in Fe^{4+} contribution across the LSFO series are linked to the expansion of FeO_6 octahedral structure, as evidenced by the increasing equivalent ionic radius (EIR) of Fe from LSFO-04 to LSFO-06 (Table S4), consistent with the XRD results. In LSMO, the Mn^{3+}/Mn^{4+} ratio in LSMO is 0.802: 0.198 (Fig. S8 and Table S3). The increased proportion of Fe^{2+} in LSFO series suggests a stronger self-reduction/defect compensation tendency, while LSMO tends toward cationic valence state compensation. These differences in valence compensation mechanisms significantly influence oxygen vacancy formation and the reducibility of the oxygen sublattice, directly affecting oxygen adsorption, dissociation, and incorporation in the ORR. Furthermore, the O 1*s* spectra (Fig. 3(b)) resolve four distinct oxygen species: lattice oxygen (O_{lat}), highly oxidative oxygen species (O^-/O_2^{2-}), surface hydroxyl group and/or carbonate (OH^-/CO_3^{2-}), and adsorbed molecular water (H_2O) [33]. The ratio of O^-/O_2^{2-} (associated with the oxygen-vacancy-related surface component) to O_{lat}, indicative of the relative abundance of oxygen-vacancy-related surface species, increases significantly from 0.17 in LSMO to 1.57 in LSFO (Table S5) [15, 34, 35]. LSFO exhibits the highest relative proportion of oxygen-vacancy-related surface oxygen species among the LSFO series samples (1.16 for LSFO-04 and 0.63 for LSFO-06), enhancing oxygen adsorption and activation at the cathode surface [36, 37]. Moreover, the electronic conductivity (EC) measurements demonstrate a marked increase with temperature, exhibiting a typical semiconductor-like behavior in ionic-electronic conductors (Fig.

3(c)). LSFO-06 displays the highest conductivity among the samples, reaching 43.83 S cm^{-1} at 800 °C, followed by 39.91 S cm^{-1} and 40.15 S cm^{-1} for LSFO-04 and LSFO (Table S6). This trend correlates with the optimal synergy of Fe^{2+}/Fe^{3+} and Fe^{3+}/Fe^{4+} redox couples with the highest (Fe^{2+} + Fe^{4+}) proportion in LSFO-06 (Table S3). All LSFO-04, LSFO, LSFO-06 samples show significantly enhanced EC and lower conduction barrier (Fig. S9) compared with LSMO. In contrast, LSMO exhibits substantially lower conductivity across temperatures, with only 10.13 S cm^{-1} at 800 °C (Table S6). The higher activation energy (Ea) for LSMO (0.29 eV) confirms less conductive than LSFO series materials, which possess the Ea values of 0.19, 0.15 and 0.13 eV for LSFO-04, LSFO and LSFO-06, respectively. ECR curves over time show that LSFO exhibits the fastest conductivity recovery. The oxygen surface exchange coefficient (K_O) and bulk diffusion coefficient (D_O) for LSFO are 2.3-15.7 times higher than those for LSMO (Fig. 3(d), Fig. S10(a), Fig. S10(c) and Table S7). Proton conductivity equilibrium is reached in just 150 s for LSFO, much faster than the 1500 s required for LSMO (Fig. 3(e), Fig. S10(b), Fig. S10(d) and Table S7). The apparent proton-related surface exchange coefficient (K_H) and diffusion coefficient (D_H) are also significantly higher for LSFO (3.7×10^{-3} cm s^{-1} and 2.3×10^{-4} cm^2 s^{-1}) compared to LSMO (3.4×10^{-4} cm $s^{-1}$and 2.2×10^{-5} cm^2 s^{-1}), demonstrating superior proton mobility in LSFO, which contributes to its enhanced ORR catalytic performance. The fitted D values may include contributions from both lattice and grain-boundary transport, which cannot be independently separated from a single conductivity-relaxation transient, whereas K may include surface reaction, incorporation, and near-surface transport contributions. Nevertheless, all samples were tested using comparable geometries and identical measurement and fitting procedures, allowing reliable comparison of their relative oxygen/proton exchange and transport kinetics. Fig. 3(f) summarizes these experimental results and reveals a non-monotonic dependence of the physicochemical and transport properties on the La/Sr ratio. These trends can be rationalized by composition-induced changes in the Fe-valence distribution, lattice structure, surface defect chemistry, electronic conductivity, and oxygen/proton transport. Increasing the La content alters the Fe valence

distribution and expands the local FeO_6 framework; however, these changes do not lead to a monotonic improvement in the cathode-related properties. Although LSFO-06 possesses the highest electronic conductivity, it shows a lower relative abundance of oxygen-vacancy-related surface species and slower oxygen/proton exchange and diffusion than LSFO. The intermediate LSFO composition therefore provides a more favorable balance among Fe redox chemistry, surface defect availability, electronic conduction, and oxygen/proton transport, which supports its enhanced p-ORR kinetics and electrochemical performance.

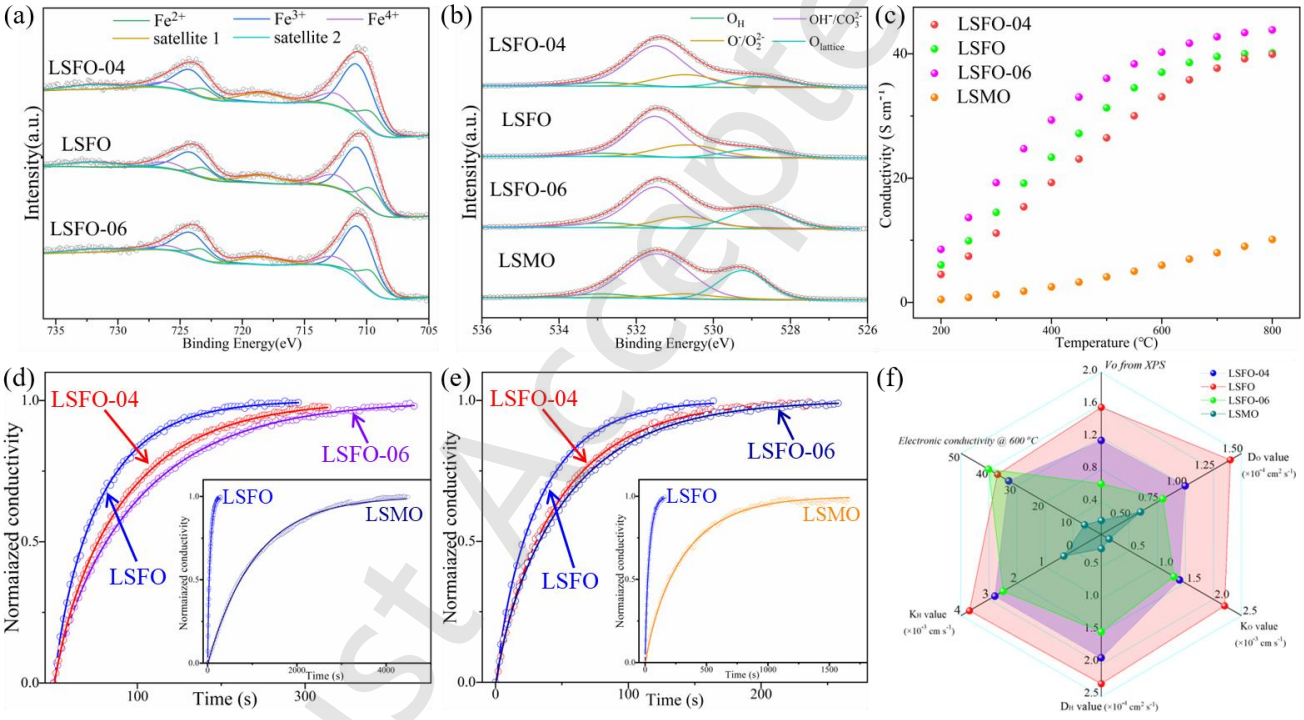

Fig. 3 Experimental validation of surface chemistry and oxygen/proton transport. XPS spectra of (a) Fe 2*p*, and (b) O 1*s*; (c) EC measurements for LSFO-04, LSFO, LSFO-06, and LSMO samples at 200-800 °C; ECR results for four samples at 600 °C under the conditions: (d) a rapid transition from air to oxygen (50% N_2) and (e) a sudden switch from dry air to wet air; (f) comparison of key physicochemical and transport properties.

3.4 Verification of accelerated p-ORR kinetics by P_{O2}/P_{H2O}-dependent EIS

The accelerated p-ORR kinetics of LSFO were further verified using symmetrical-cell EIS under controlled oxygen and water-vapor partial pressures (P_{O2} and P_{H2O}) at 600 °C. LSFO (Fig. 4(a)-(b))

shows a significantly lower area-specific resistance (ASR) than LSMO (Fig. S11(a)-(b)), confirming that the electronic-structure and transport advantages identified above translate into faster cathodic reaction kinetics. As P_{O2} increases, the overall polarization resistance decreases, indicating that oxygen adsorption, dissociation, surface exchange, and diffusion participate in the rate-determining processes, and providing valuable insights into the ORR dynamics. EIS deconvolution, using the equivalent circuit $R(R_HQ_H)(R_MQ_M)(R_LQ_L)$, identifies three distinct ORR processes: high frequency process (R_H, corresponding to charge transfer), middle-frequency process (R_M, associated with ORR), and low-frequency process (R_L, representing surface diffusion of oxygen species) [38, 39], which is related to the characteristic frequency ranges. The relationship $R_P = k(P_{O2})^{-n}$ (where n could be interpreted as apparent pressure-dependence coefficients of the corresponding frequency-domain resistance components) [40] shows that all R_H, R_M, R_L processes for LSFO are dependent with P_{O2}, with n values of 0.13, 0.28 and 1.2 (Fig. 4(c)). Similarly, for LSMO, R_M shows a stronger dependence on P_{O2} (n = 0.79), suggesting a greater contribution of oxygen-related processes to these frequency-domain responses (Fig. S11(c)). When steam was introduced, the electrochemical system became more complex, involving concurrent processes of oxygen diffusion, steam transport, and ionic conduction. The ASR for both samples exhibits a clear dependence on P_{H2O}, indicating protonation. The hydration reaction facilitates proton generation and migration, thereby increasing the number of protons available for ORR at electrode surface. As a result, electrode performance improves under high steam concentrations due to enhanced proton conductivity and accelerated ORR kinetics [41]. Similarly, R_H and R_M are associated with ion transfer across interface, and surface exchange ($V_O^{\bullet\bullet} + H_2O + O_O^{\times} \rightarrow 2OH_O^{\bullet}$, $2V_O^{\bullet\bullet} + O_2 \rightarrow 2O_O^{\times} + 4h^{\bullet}$), while R_L represents the mass transfer process [42]. The relationship between R_P and P_{H2O} follows the expression: $R_P = k(P_{H2O})^{-m}$. In LSFO, all three electrode processes exhibit stronger dependence on P_{H2O} with m values of 0.41, 0.51 and 0.36 (Fig. 4(d)), while LSMO shows similar behaviour but with slighter lower dependence (m values of 0.37, 0.22, 0.29 for R_H, R_M, and R_L, refer to Fig. S11(d)). LSFO significantly decreases all R_H, R_M, R_L values in both water and

oxygen environment (Fig. S12), outperforming LSMO in all ORR sub-processes. These results demonstrate that LSFO does not only improve a single elementary step; rather, it accelerates the coupled oxygen and proton reaction sequence required for PCFC cathodes.

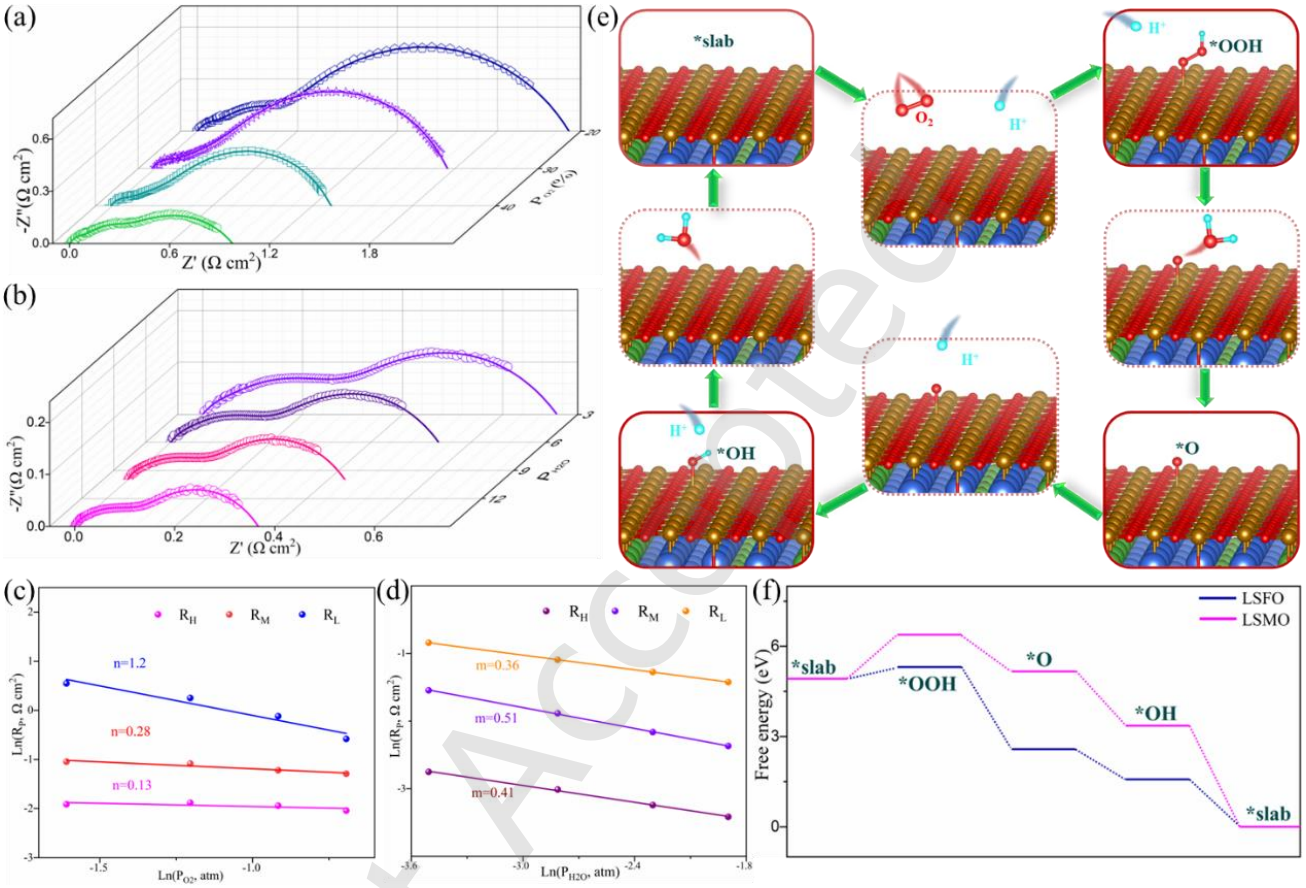

Fig. 4 Verification of accelerated p-ORR kinetics. EIS of LSFO symmetrical cells under different (a) P_{O2} and (b) P_{H2O}, and the dependence of polarization resistance at LF, MF, and HF as a function of (c) P_{O2} and (d) P_{H2O}; (e) Schematic illustrations of ORR steps and (f) the corresponding standard free energies on the surface of LSFO and LSMO.

The computed free energies (ΔG) for the ORR steps further support these findings, serving as thermodynamic indicators of ORR activity. The ORR processes at the PCFC cathodes involve proton combination and water release at the cathode, which includes the generation of *OOH, *O, and *OH intermediates (Fig. 4(e)). Calculating ΔG for each step provides insights into the thermodynamic difficulty of the reaction pathway of the ORR process. As shown in Fig. 4(f), *OOH represents the

potential rate-limiting step for both cathodes, with energy barriers of 0.39 eV for LSFO and 1.46 eV for LSMO. The substantially smaller value for LSFO indicates more effective stabilization of the *OOH intermediate on the Fe-based surface, which is associated with the smaller Fe 3d-O 2p energy separation, stronger orbital hybridization, and more favorable oxygen-defect chemistry of LSFO, which facilitate interfacial charge redistribution and oxygen-species activation. Furthermore, the energy steps for the formation of *O and *OH are thermodynamically favorable in LSFO, suggesting these steps are energetically easier to achieve compared to LSMO. Overall, the lower ORR free-energy barrier is consistent with the stronger Fe 3d-O 2p interaction, easier oxygen-defect formation, and faster proton migration predicted by DFT. Therefore, the P_{O2}-/P_{H2O}-dependent EIS and ORR energetics jointly confirm that LSFO possesses intrinsically enhanced p-ORR activity.

3.5 Cell-level performance, durability, and microstructural verification

The cell-level performance was evaluated to determine whether the DFT-predicted and experimentally validated kinetic advantages of LSFO can be translated into practical PCFC output. As depicted in Fig. 5(a), the LSFO cell achieved remarkable peak power densities (PPDs) of 2192, 1477, 853 and 465 mW cm^{-2} at 700-550°C, significantly outperforming the LSFO-04 and LSFO-06 cell (Fig. 5(b)-(c) and Fig. S13(a)-(c)). These values also exceed those of LSMO, which recorded PPDs of 1050, 727, 464, and 285 mW cm^{-2} under the same conditions (Fig. S13(d)), representing a performance enhancement of 108.76%, 103.16%, 83.84%, and 63.16%, respectively, as shown in Table S8, which demonstrates a catalytically amplified effect. The LSFO cell also outperforms many state-of-the-art Ln_2NiO_4-based and R-P cathodes in terms of PPDs (Fig. 5(d)). Furthermore, LSFO exhibited acceptable durability, maintaining stable performance for over 400 hours with minimal degradation of 3.2% per 1000 h (0.03 mV h^{-1}, Fig. 5(e)), demonstrating that the high performance is not a transient activation effect but a durable cathodic advantage. To further evaluate the chemical stability of LSFO, the LSFO-BZCY composite was treated in humid air for 400 h. The aged composite retained the characteristic XRD reflections of both LSFO and BZCY without detectable secondary phases (Fig.

S14(a)), indicating good chemical compatibility under the investigated conditions. XPS analysis of LSFO after the same humid-air treatment gave La, Sr, Fe, O, and C atomic percentages of 3.53%, 10.11%, 7.02%, 49.08%, and 30.25%, respectively (Fig. S14(b)-(c)). The corresponding surface Sr enrichment factor, defined as $EF_{\mathrm{Sr}} = (\mathrm{Sr/Fe})_{\mathrm{XPS}}/(\mathrm{Sr/Fe})_{\mathrm{nominal}}$, was approximately 0.96, suggesting no appreciable Sr surface enrichment. The atomic fractions of Fe^{2+}, Fe^{3+}, Fe^{4+} were 0.146, 0.719, and 0.135 (Fig. S14(d)), showing no obvious change in the Fe valence distribution. In addition, the EIS spectra (Fig. S14(e)) before and after the durability test were also recorded comparatively, in which the high-frequency intercept of the Nyquist plots determined the ohmic resistance (R_O), while the total polarization resistance (R_P) was derived from the difference between the high- and low-frequency intercepts. It retained similar overall profiles, without the appearance of an obvious additional impedance arc. R_O increased only slightly from 0.105 to 0.106 Ω cm^2, while R_P increased from 0.209 to 0.215 Ω cm^2, corresponding to the increases of approximately 1% and 2.87%, respectively. These limited changes indicate that the ohmic transport, electrode/electrolyte contact, and cathodic polarization behavior were largely maintained during operation, supporting that the high performance was not merely a transient activation effect. Moreover, post-operation cross-sectional SEM-EDS mapping (Fig. S15) revealed that Ba/Ce and La/Sr/Fe remained primarily confined to the electrolyte and cathode regions, without obvious elemental interdiffusion or formation of a continuous interfacial reaction layer. These results support the phase, surface-chemical, and interfacial stability of LSFO during 400 h stability test.

EIS (Fig. 5(f) and Fig. S16(a)) were further evaluated to validate the enhanced catalytic activity. LSFO-based cells consistently demonstrated lower R_O and R_P values compared to the LSMO cell at all tested temperatures (Table S9), indicating reduced polarization losses and accelerated reaction kinetics. This performance improvement is attributed to enhanced electron transfer efficiency and optimized charge transfer processes in LSFO materials, significantly lowering cathode resistance and contributing to the overall performance. Because R_O includes electrolyte, contact, current-collection,

and interfacial transport contributions, its lower value in LSFO cells may mainly arise from improved cathode-side electronic/ionic transport and interfacial transport continuity. The improved charge transfer is further supported by better ORR kinetics, which facilitate efficient oxygen ion transport at the electrolyte-cathode interface and accelerate proton migration. Significantly, the LSFO performs the best, possessing R_O of 0.065, 0.083, 0.105, 0.135 Ω cm^2 and R_P of 0.040, 0.078, 0.21, 0.639 Ω cm^2 at 700-550 °C, respectively, demonstrating optimal cathode electrocatalytic behavior. This non-monotonic performance trend is consistent with the physicochemical and transport results discussed above, confirming that the intermediate LSFO composition achieves a more favorable balance among electronic conduction, surface defect chemistry, and oxygen/proton transport, thereby delivering the lowest R_P and highest PPDs among Fe-based compositions. Distribution of relaxation time (DRT) analysis (Fig. 5(g) and Fig. S16(b)) revealed three distinct peaks, corresponding to proton transfer (high-frequency peak), oxygen reduction and ionic diffusion (medium-frequency peak), and gas-phase diffusion/oxygen surface adsorption/dissociation processes (low-frequency peak) [38, 39, 43, 44]. Narrower peaks in LSFO cells suggest more efficient reaction pathways, a marked improvement over LSMO cells, which is also confirmed by the DRT analysis (Fig. S17). Arrhenius plots (Fig. 5(h) and Fig. S18) further validated thermally activated mechanisms, showing higher Ea values for R_P in LSFO-04 (1.40 eV), LSFO (1.29 eV), and LSFO-06 (1.48 eV), compared to LSMO (1.10 eV). However, LSFO-based cells exhibited significantly lower resistance values, confirming their superior electrocatalytic performance. Additionally, equivalent circuit fitting with an $LR(R_HQ_H)(R_MQ_M)(R_LQ_L)$ model (Fig. S16(c)) confirmed enhanced oxygen adsorption/dissociation (R_L), improved charge transfer (R_M, $O_{ad} + e^- \rightarrow O_{ad}^-$, $O_{ad}^- + e^- \rightarrow O_{ad}^{2-}$), and better proton mobility (R_H), as given in Table S10, leading to rapid ORR kinetics. These kinetic advantages are also consistent with the Fe-valence characteristics discussed above, where the relatively lower average B-site valence associated with Fe^{2+} incorporation (Table S11) indicates a modified Fe redox environment that may favor balanced electronic and ionic transport. Consequently, LSFO exhibits the lowest R_O and R_P values among the

Fe-based compositions. Accompanied with the relatively low Ea values for all resistances (R_L, R_M, R_H) (Fig. 5(h)), it supports the superior overall electrocatalytic performance.

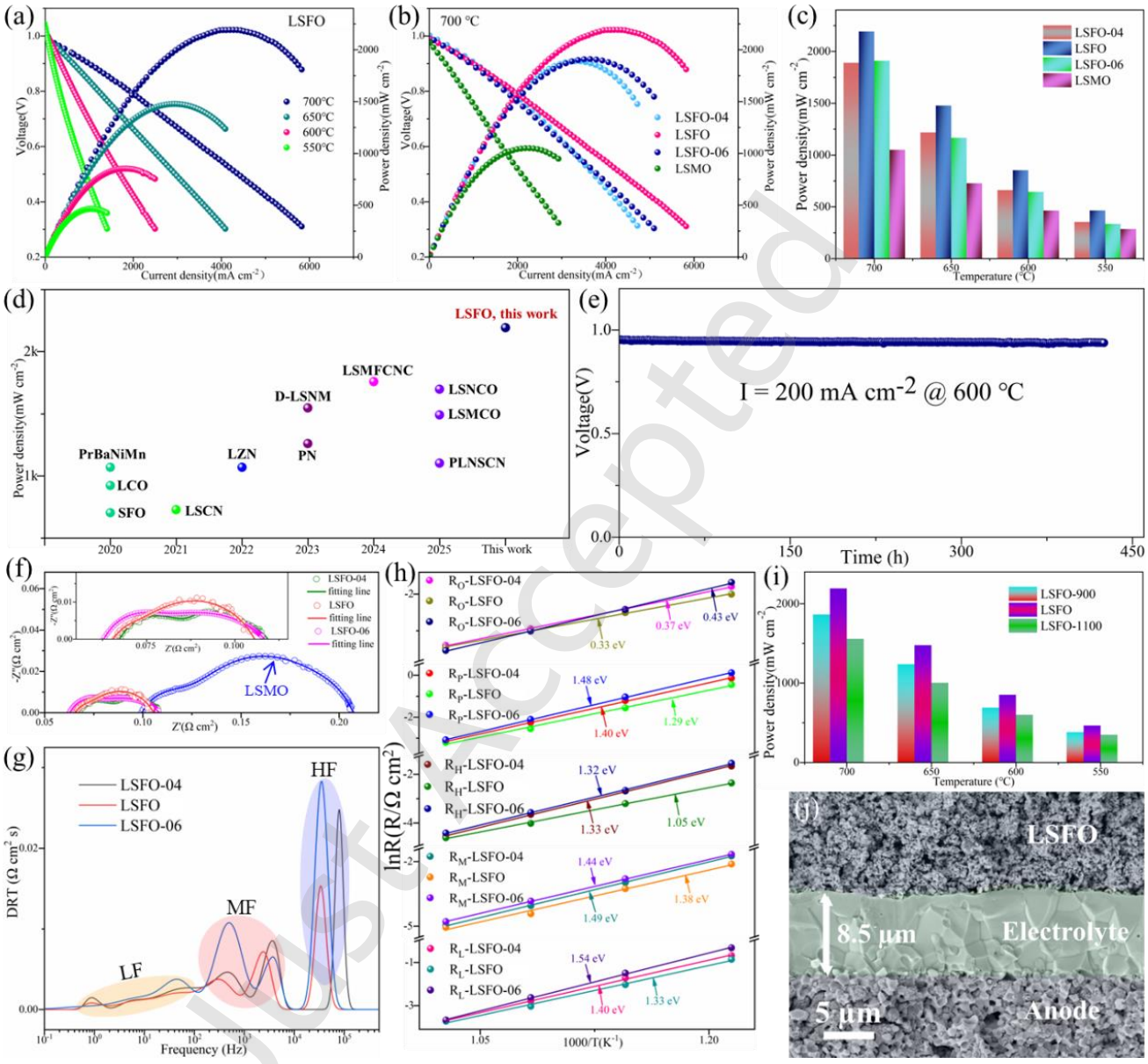

Fig. 5 Cell-level performance and microstructural verification. Power curves of (a) LSFO cell, (b) cells with different cathodes at 700 °C, and (c) the corresponding PPD comparison; (d) Power output benchmarking against reported single Ln_2NiO_4-based cathodes, and representative R-P cathodes for $BaCeO_3$-based cells at 700 °C (fuel: H_2 with 3% H_2O, oxidant: ambient air, current collector: Ag paste, d: cell electrolyte thickness, LSFO: this work, LSNCO: $La_{1.2}Sr_{0.8}Ni_{0.5}Co_{0.5}O_{4+\delta}$, d = 7 μm [45], LSMCO: $La_{0.5}Sr_{1.5}Mn_{0.8}Co_{0.2}O_{4+\delta}$, d = 10.6 μm [46], PLNSCN: $(Pr_{0.25}La_{0.25}Nd_{0.25}Ca_{0.25})_2NiO_{4+\delta}$, d =

10 μm [47], LSMFCNC: $La_{1.2}Sr_{0.8}Mn_{0.2}Fe_{0.2}Co_{0.2}Ni_{0.2}Cu_{0.2}O_{4+\delta}$, d = 7.4 μm [48], PN: $Pr_4Ni_3O_{10+\delta}$, d = 15 μm [49], D-LSNM: $(La_{1.2}Sr_{0.8})_{0.9}Ni_{0.5}Mn_{0.5}O_4$, d = 5.4 μm [50], LZN: $La_2Ni_{0.75}Zn_{0.25}O_4$, d = 10.5 μm [51], LSCN: $La_{1.6}Sr_{0.4}Cu_{0.6}Ni_{0.4}O_{4+\delta}$, d = ~10 μm [52], PrBaNiMn: $Pr_2BaNiMnO_7$, d = 12 μm [53], LCO: $La_{1.5}Ca_{0.5}NiO_{4+\delta}$, d = 16 μm [54], SFO: $Sr_3Fe_2O_7$, d = ~13 μm [55]); (e) The durability estimation of LSFO cell at 600 °C (fuel: humid H_2, oxidant: ambient air, applied current density: 200 mA cm^{-2}); (f) EIS of cells with different cathodes at 700 °C under open-circuit voltage, and (g) the corresponding DRT analysis; (h) temperature-dependent resistance (R_O, R_P, R_H, R_M, R_L) comparison via Arrhenius plots; Comparison of (i) PPD between the tested LSFO-900, LSFO and LSFO-1100 cells; (j) Post-operation cross-sectional SEM microstructure characterization of LSFO cell.

The cathode sintering temperature was further optimized to exclude microstructural artifacts and identify the most effective electrode preparation condition. LSFO cathodes prepared at 900, 1000 and 1100 ℃ were denoted as LSFO-900, LSFO and LSFO-1100, respectively. The LSFO cell demonstrates significantly higher PPDs than both the LSFO-900 and LSFO-1100 cell (Fig. 5(i), Fig. S19(a)-(b) and Table S12). At testing temperature range, the PPD performance shows slower degradation with increasing cathode calcination temperature (Fig. S20). EIS data further confirm the optimal performance of the LSFO cell, with the lowest R_O and R_P values (Fig. S21, Fig. S22(a) and Table S13), indicating faster ORR processes. DRT analysis in different frequency ranges (Fig. S22(b)) support these findings. Though the R_P contribution increases with cathode calcination temperature (Fig. S23), the lowest R_O and R_P values for LSFO (Table S13) ensure optimal cell performance, leading to exceptional power density.

Post-operation SEM (Fig. 5(j) and Fig. S24) reveal similar microstructures across LSFO-04, LSFO, LSFO-06, and LSMO cells, indicating that the performance improvements stem from species transport optimization, rather than microstructural concerns. The tight adhesion between the cathodes and electrolytes ensure efficient interface reactions, while the well-connected cathode particles networks (Fig. S25) facilitate gas diffusion and electrochemical activity. It should also be noted that LSFO-based

cathodes possess larger average particles (average sizes of 214 nm, 216 nm, and 213 nm for LSFO-04, LSFO, and LSFO-06, Fig. S26) compared to LSMO (153 nm, Fig. S26), which may reduce the effective triple-phase boundaries and electrochemically active reaction interfaces to some extent, making surface-related processes, gas diffusion, and interfacial charge transfer more temperature-sensitive at lower temperatures. This is consistent with the higher Ea values for LSFO-based cathodes discussed before. Nonetheless, LSFO-based cathodes still exhibit remarkably enhanced cell performance. Furthermore, although the LSFO-900 and LSFO-1100 cell had a thinner electrolyte (Fig. S27), its superior performance in LSFO demonstrate that an appropriate cathode calcination temperature enhances electrocatalytic activity. The optimized microstructure (Fig. S25(b) and Fig. S28(a)-(b)) and particle size (179 nm for LSFO-900, 216 nm for LSFO, 262 nm for LSFO-1100, refer to Fig. S26(b) and Fig. S28(c)-(d)) were crucial for ensuring effective cathode reactions. Despite the finer particles in LSFO-900, it may suffer from insufficient particle necking, discontinuous transport pathways, and weaker cathode/electrolyte contact. In contrast, excessive coarsening in LSFO-1100 reduces the active surface and interfacial areas. Thus, the superior performance of LSFO arises from a more favorable balance among particle size, connectivity, porosity, and interfacial adhesion. Taken together, the DFT, ECR, EIS/DRT, durability, and microstructural results establish a consistent electronic structure-defect-transport-performance relationship for LSFO. Its enhanced electrochemical performance should not be attributed solely to the d-band center or Fe 3d-O 2p alignment, because these descriptors are closely coupled with oxygen nonstoichiometry, Fe valence distribution, local lattice distortion, surface defect chemistry, electronic/ionic transport, and electrode microstructure. The smaller d-p energy separation and stronger Fe-O hybridization provide a favorable electronic basis for oxygen-defect formation, hydration-related proton incorporation, and interfacial charge redistribution. Together with the higher electronic conductivity, faster oxygen/proton exchange and diffusion, and favorable cathode/electrolyte interfacial contact of LSFO, these coupled factors contribute to its enhanced p-ORR kinetics and cell performance. Therefore, coordinated regulation of

the d-band center and Fe 3d-O 2p alignment, when considered together with the associated defect, transport, and microstructural properties, provides an effective approach for improving K_2NiF_4-type cathodes for PCFCs.

4 Conclusions

Regulating d-band center and d-p orbital alignment in electrode design is an effective approach for improving the electrocatalytic performance of electrode materials. In this study, Fe-based K_2NiF_4-type LSFO cathodes were developed through a DFT-guided electronic-structure regulation and evaluated as high-performance cathodes for PCFCs. The superior performance of LSFO does not originate from the negligible work-function difference between LSFO and LSMO, but from the more favorable Fe 3d-O 2p orbital alignment and oxygen-redox activity produced by Fe-based B-site chemistry. DFT calculations reveal that this regulated electronic structure lowers the energetic cost of oxygen-vacancy formation, improves hydration-related proton incorporation, reduces the proton-hopping barrier, and decreases the free-energy barrier for key ORR intermediates. These predictions are experimentally validated by XPS, EC, and ECR results, which show enriched oxygen-vacancy-related surface species, higher electronic conductivity, and faster oxygen/proton surface exchange and bulk diffusion in LSFO. P_{O2}/P_{H2O}-dependent EIS further confirms that LSFO accelerates multiple p-ORR sub-processes. Consequently, the optimized LSFO cathode achieves PPDs of 2192 and 853 mW cm^{-2} at 700 and 600 °C, respectively, with corresponding R_P values of 0.04 and 0.21 Ω cm^2. The LSFO cell also exhibits stable operation over 400 h and maintains a robust post-test microstructure. This work demonstrates that coordinated regulation of the d-band center and d-p orbital alignment provides a useful basis for developing advanced R-P cathodes with rapid p-ORR kinetics.

Acknowledgements

This work was supported by the National Natural Science Foundation of China (Grant Nos: 51802200) and the Startup Funding for Talents at University of South China. The authors acknowledge the technicians at Shenzhen HUASUAN Technology Co., Ltd. for assistance with theoretical calculations.

Author contributions

Zhe Song: Conceptualization, Investigation, Formal analysis, Software

Shaozhi Wang: Conceptualization, Data curation, Methodology, Writing -original draft

Dezhi Geng: Methodology, Investigation, Validation

Zhangjin Xie: Validation, Visualization, Software

Shenchi Qu: Project administration, Writing-review & editing

Jie Hou: Supervision, Funding acquisition, Resources

Availability of data and materials

The data that support the findings of this study are available from the corresponding author upon reasonable request.

Competing interests

The authors have no competing interests to declare that are relevant to the content of this article.

Electronic Supplementary Material (ESM)

Supplementary material is available in the online version of this article.

References

[1] Wang Z, Wang Y, Wang J, et al. Rational design of perovskite ferrites as high-performance proton-conducting fuel cell cathodes. Nature Catalysis. 2022,5:777-787.
[2] Zhang Y, Chen B, Guan D, et al. Thermal-expansion offset for high-performance fuel cell cathodes. Nature. 2021,591:246-251.

[3] Jiang C, Ma J, Corre G, Jain SL, Irvine JTS. Challenges in developing direct carbon fuel cells. Chemical Society Reviews. 2017,46:2889-2912.
[4] Gao Z, Mogni LV, Miller EC, Railsback JG, Barnett SA. A perspective on low-temperature solid oxide fuel cells. Energy Environ. Sci. 2016,9:1602-1644.
[5] Li T, Yang Y, Yang F, et al. High-oxygen vacancy cerium catalysts with NiFe alloy heterostructures: A pathway for efficient and stable biomass ethanol fuel tubular solid oxide fuel cells. Journal of Advanced Ceramics. 2025,14:9221143.
[6] Liu C, Liu B, Li Z, et al. Interface-engineering to boost the performance and durability of nickel-metal-supported reversible proton ceramic cells for power generation and hydrogen production. Journal of Advanced Ceramics. 2025,14:9221115.
[7] Bian W, Wu W, Wang B, et al. Revitalizing interface in protonic ceramic cells by acid etch. Nature. 2022,604:479-485.
[8] Jiang S, Zheng X, Sun W. Toward Advanced Fuel Electrodes for High-Performance Proton-Conducting Ceramic Cells. Advanced Energy Materials. 2025,15:2403745.
[9] Yin Y, Huang H, Boulfrad S, et al. Breaking the limits of Ruddlesden–Popper cathodes to achieve a game-changer for proton-conducting solid oxide fuel cells. Energy & Environmental Science. 2025,18:8130-8141.
[10] Song W, Dong X, Yin Y, et al. Reviving the activity of Si-contaminated cathodes via chloride anion doping for proton-conducting solid oxide fuel cells. Journal of Advanced Ceramics. 2026,15:9221262.
[11] Zhang X, Wang C, Liu K, et al. Significantly enhanced stability and activity of a perovskite oxygen electrode for reversible protonic ceramic electrochemical cells by heterointerface engineering. Journal of Advanced Ceramics. 2025,14:9221108.
[12] Deng M, Wang S, Song Z, et al. B-site compositional-complexity-mediated defect regulation in manganite-based K2NiF4-type cathodes for high performance protonic ceramic fuel cells. Fuel. 2027,428:140568.
[13] Yin Y, Liu B, Yan D, et al. Balancing intrinsic properties of cathode materials allows high performance for protonic ceramic fuel cells. SusMat. 2024,4:e240.
[14] Gong J, Du K, Jiang W, et al. Controlled growth of $Pr_{1.5}Ba_{1.5}Cu_3O_7$ cubes to meliorate the cathode reaction for protonic ceramic fuel cells. Journal of Advanced Ceramics. 2025,14:9221060.
[15] Zhou R, Yin Y, Dai H, Yang X, Gu Y, Bi L. Attempted preparation of $La_{0.5}Ba_{0.5}MnO_{3-\delta}$ leading to an in-situ formation of manganate nanocomposites as a cathode for proton-conducting solid oxide fuel cells. Journal of Advanced Ceramics. 2023,12:1189-1200.
[16] Chen X, Tan Y, Li Z, et al. Advanced Air Electrodes for Reversible Protonic Ceramic Electrochemical Cells: A Comprehensive Review. Advanced Materials. 2025,37:2418620.
[17] Tarutin AP, Lyagaeva JG, Medvedev DA, Bi L, Yaremchenko AA. Recent advances in layered $Ln_2NiO_{4+\delta}$ nickelates: fundamentals and prospects of their applications in protonic ceramic fuel and electrolysis cells. Journal of Materials Chemistry A. 2021,9:154-195.
[18] Zhang S, Dou Y, Xia T, et al. Achieving electrocatalytic activity toward oxygen reduction reaction based on Ruddlesden–Popper type cathode catalyst for solid oxide fuel cells. Journal of Advanced Ceramics. 2025,14:9221178.
[19] Xie Z, Song Z, Wu Y, et al. Coupling defect chemistry and configurational entropy to enhance cathode electrocatalysis in protonic ceramic fuel cells. Acta Materialia. 2026,315:122368.
[20] Zhu X, Tan X, Wu K-H, et al. Intrinsic ORR Activity Enhancement of Pt Atomic Sites by Engineering the d-Band Center via Local Coordination Tuning. Angewandte Chemie International Edition. 2021,60:21911-21917.
[21] Zhou Y, Zhou Z, Shen R, et al. Correlating electrocatalytic oxygen reduction activity with d-band centers of metallic nanoparticles. Energy Storage Materials. 2018,13:189-198.
[22] Ou L. Design of Pd-Based Bimetallic Catalysts for ORR: A DFT Calculation Study. Journal of Chemistry. 2015,2015:932616.
[23] Gao X, Liu H, Wang Y, et al. Tailoring the d-band electronic structure of deficient $LaMn_{0.3}Co_{0.7}O_{3-\delta}$ perovskite nanofibers for boosting oxygen electrocatalysis in Zn-Air batteries. Journal of Colloid and Interface Science. 2023,650:951-960.
[24] Zhang W, Wang S, Yang C, et al. Dual-Donor Doped Perovskite as Bifunctional Oxygen Electrode Catalyst for Reversible Protonic Ceramic Electrochemical Cell. Journal of the American Chemical Society. 2025,147:43584-43593.
[25] Hou J, Gong J, Luo J-L. Constructing highly active surface-nanostructured core/bi-shell $La_{1.2}Sr_{0.8}Ni_{0.5}Mn_{0.5}O_{4+\delta}$ cathode for protonic ceramic fuel cells. Chemical Engineering Journal. 2023,459:141459.
[26] Gao J, Liu Y, Gao Y, et al. Cobalt-free fluorine doped $Bi_{0.7}Sr_{0.3}FeO_{3-\delta}$ oxides for energetic cathodes of low-temperature solid oxide fuel cells. Chemical Engineering Journal. 2023,452:139584.
[27] Ren R, Yu X, Wang Z, et al. Fluorination inductive effect enables rapid bulk proton diffusion in $BaCo_{0.4}Fe_{0.4}Zr_{0.1}Y_{0.1}O_{3-\delta}$ perovskite oxide for high-activity protonic ceramic fuel cell cathode. Applied Catalysis B: Environmental. 2022,317:121759.
[28] Huang YL, Pellegrinelli C, Lee KT, Perel A, Wachsman ED. Enhancement of $La_{0.6}Sr_{0.4}Co_{0.2}Fe_{0.8}O_{3-\delta}$ Surface Exchange through Ion Implantation. Journal of The Electrochemical Society. 2015,162:F965.
[29] Kresse G, Furthmüller J. Efficient iterative schemes for ab initio total-energy calculations using a plane-wave basis set. Physical Review B. 1996,54:11169-11186.

[30] Xi X, Liu J, Fan Y, et al. Reducing d-p band coupling to enhance CO_2 electrocatalytic activity by Mg-doping in Sr2FeMoO6-δ double perovskite for high performance solid oxide electrolysis cells. Nano Energy. 2021,82:105707.
[31] Wu X, Yu Y, Chen Y, et al. Construction of Multifunctional Nanoarchitectures in One Step on a Composite Fuel Catalyst through In Situ Exsolution of $La_{0.5}Sr_{0.5}Fe_{0.8}Ni_{0.1}Nb_{0.1}O_{3-\delta}$. ACS Applied Materials & Interfaces. 2020,12:34890-34900.
[32] Bai J, Niu L, Zhu Q, et al. Ni-doped Fe-based perovskite to obtain multifunctional and highly efficient electrocatalytic active IT-SOFC electrode. Fuel. 2024,365:131334.
[33] Zhang X, Pei C, Chang X, et al. FeO_6 Octahedral Distortion Activates Lattice Oxygen in Perovskite Ferrite for Methane Partial Oxidation Coupled with CO2 Splitting. Journal of the American Chemical Society. 2020,142:11540-11549.
[34] Yin Y, Zhou Y, Gu Y, Bi L. Successful preparation of $BaCo_{0.5}Fe_{0.5}O_{3-\delta}$ cathode oxide by rapidly cooling allowing for high-performance proton-conducting solid oxide fuel cells. Journal of Advanced Ceramics. 2023,12:587-597.
[35] Li Y, Xu Y, Yin Y, et al. Entropy engineering design of high-performing lithiated oxide cathodes for proton-conducting solid oxide fuel cells. Journal of Advanced Ceramics. 2023,12:2017-2031.
[36] Gong J, Hou J. Restoring $La_{1.2}Sr_{0.8}Ni_{0.5}Mn_{0.5}O_{4+\delta}$ electrocatalysis for proton-conducting solid oxide fuel cells with the elimination of bi-shell surface. Applied Surface Science. 2023,640:158385.
[37] Zhu Y, Zhou W, Yu J, et al. Shao Z. Enhancing Electrocatalytic Activity of Perovskite Oxides by Tuning Cation Deficiency for Oxygen Reduction and Evolution Reactions. Chemistry of Materials. 2016,28:1691-1697.
[38] Fabbri E, Bi L, Pergolesi D, et al. High-performance composite cathodes with tailored mixed conductivity for intermediate temperature solid oxide fuel cells using proton conducting electrolytes. Energy & Environmental Science. 2011,4:4984-4993.
[39] He F, Wu T, Peng R, et al. Cathode reaction models and performance analysis of $Sm_{0.5}Sr_{0.5}CoO_{3-\delta}$–$BaCe_{0.8}Sm_{0.2}O_{3-\delta}$ composite cathode for solid oxide fuel cells with proton conducting electrolyte. Journal of Power Sources. 2009,194:263-268.
[40] Xu Y, Xu K, Zhang H, et al. An efficient electrode for reversible oxygen reduction/evolution and ethylene electro-production on protonic ceramic electrochemical cells. Science Bulletin. 2024,69:3682-3691.
[41] Xu Y, Xu K, Zhu F, et al. A Low-Lewis-Acid-Strength Cation Cs^+-Doped Double Perovskite for Fast and Durable Oxygen Reduction/Evolutions on Protonic Ceramic Cells. ACS Energy Letters. 2023,8:4145-4155.
[42] Ren R, Wang Z, Xu C, et al. Tuning the defects of the triple conducting oxide $BaCo_{0.4}Fe_{0.4}Zr_{0.1}Y_{0.1}O_{3-\delta}$ perovskite toward enhanced cathode activity of protonic ceramic fuel cells. Journal of Materials Chemistry A. 2019,7:18365-18372.
[43] Wu S, Xu X, Li X, Bi L. High-performance proton-conducting solid oxide fuel cells using the first-generation Sr-doped LaMnO3 cathode tailored with Zn ions. Science China Materials. 2022,65:675-682.
[44] Hou J, Wang Q, Li J, et al. Rational design of an in-situ co-assembly nanocomposite cathode $La_{0.5}Sr_{1.5}MnO_{4+\delta}$-$La_{0.5}Sr_{0.5}MnO_{3-\delta}$ for lower-temperature proton-conducting solid oxide fuel cells. Journal of Power Sources. 2020,466:228240.
[45] Hu J, Ma L, Jiang W, et al. Improving cathode electrocatalysis via Co-substitution-driven interstitial transport for proton-conducting solid oxide fuel cells. Materials Science and Engineering: B. 2025,319:118372.
[46] Geng D, Feng H, Ma L, et al. Modulating B-site atomic environment via Co-doping to meliorate $La_{0.5}Sr_{1.5}MnO_4$ cathode electrocatalysis for protonic ceramic fuel cells. Progress in Natural Science: Materials International. 2025,35:773-779.
[47] Kang K, Liu Y, Liu X, et al. Local lattice distortion regulation in high entropy engineering to enhance the triple conductivity of layered Ruddlesden-Popper perovskite cathode in H^+-SOFCs. Chemical Engineering Journal. 2025,507:159463.
[48] Gong J, Hou J. B-site high-entropy tailoring K_2NiF_4 oxide as an effective cathode for proton-conducting solid oxide fuel cells. Journal of Materials Science & Technology. 2024,186:158-163.
[49] Li X, Chen Z, Huan D, et al. Highly Active Cathode Achieved by Constructing Surface Proton Acid Sites through Electronic Regulation of Heteroatoms. ACS Materials Letters. 2023,5:2896-2905.
[50] Gong J, Hou J. Restoring $La_{1.2}Sr_{0.8}Ni_{0.5}Mn_{0.5}O_{4+\delta}$ electrocatalysis for proton-conducting solid oxide fuel cells with the elimination of bi-shell surface. Applied Surface Science. 2023:158385.
[51] Yang X, Xu X, Wu S, et al. Enhancing the performance of traditional La_2NiO_{4+x} cathode for proton-conducting solid oxide fuel cells with Zn-doping. Ceramics International. 2022,48:19626-19632.
[52] Ma J, Pan Y, Wang Y, et al. A Sr and Ni doped Ruddlesden−Popper perovskite oxide $La_{1.6}Sr_{0.4}Cu_{0.6}Ni_{0.4}O_{4+\delta}$ as a promising cathode for protonic ceramic fuel cells. Journal of Power Sources. 2021,509:230369.
[53] Wang Q, Hou J, Fan Y, et al. $Pr_2BaNiMnO_{7-\delta}$ double-layered Ruddlesden–Popper perovskite oxides as efficient cathode electrocatalysts for low temperature proton conducting solid oxide fuel cells. Journal of Materials Chemistry A. 2020,8:7704-7712.
[54] Gu C-Y, Wu X-S, Cao J-F, et al. High performance Ca-containing $La_{2-x}Ca_xNiO_{4+\delta}$($0\leq x\leq 0.75$) cathode for proton-conducting solid oxide fuel cells. International Journal of Hydrogen Energy. 2020,45:23422-23432.
[55] Dong K, Hou J, Miao L, et al. A comparative study of the R-P phase $Sr_{n+1}Fe_nO_{3n+1}$ (n= 1, 2 and 3) cathodes for intermediate temperature solid oxide fuel cells. Ceramics International. 2020,46:19335-19342.